Materials Advances

ROYAL SOCIETY OF CHEMISTRY

PAPER

View Article Online
View Journal

Cite this: DOI: 10.1039/d5ma00914f

Synthesis and characterization of potential $CeNiO_3$ perovskite for photoelectrochemical water splitting

Hosakote Shankar Anusha,[ab] Vodeti Rajeshwar,[c] Usha Jinendra,[d] Jagadeep Chandra S,[e] Elayaperumal Sumitha,[f] Basavarajappa Sannappa Hanumanthappa,[g] Vinod Divya,[a] Mohammad Khalid,[h] Shadma Wahab,[i] Kotermane Mallikarjunappa Anilkumar,*[a] Peter R. Makgwane,[j] Honnegowdanahalli Shivabasappa Nagendra Prasad [k] and Harikaranahalli Puttaiah Shivaraju *[abl]

Photoelectrochemical (PEC) water splitting offers a sustainable pathway for hydrogen production; however, its practical implementation is often limited by the poor efficiency and stability of photoelectrodes. In this work, porous cerium nickel oxide ($CeNiO_3$) was synthesized *via* a simple citrate sol–gel method coupled with a hydrothermal approach and employed as a photoanode for PEC water splitting. The structural, morphological, and optical characteristics of the material were comprehensively investigated using XRD, UV-vis spectroscopy, FESEM, EDX, XPS, PL, and FTIR analyses. The optimized $CeNiO_3$ photoelectrode demonstrated an excellent photocurrent density of 15.14 mA cm^{-2} at 1.4 V *vs.* RHE. Electrochemical impedance spectroscopy (EIS) revealed enhanced charge transfer kinetics and suppressed recombination of photoexcited charge carriers. The superior PEC activity of $CeNiO_3$ is attributed to its bimetallic interactions, strong solar light absorption, efficient charge separation, and rapid charge transport. These results highlight the potential of $CeNiO_3$ as a stable and efficient photoelectrode for solar-driven hydrogen generation.

Received 16th August 2025,
Accepted 7th November 2025

DOI: 10.1039/d5ma00914f

rsc.li/materials-advances

[a] Department of Environmental Sciences, JSS Academy of Higher Education and Research, Mysuru, 570015, India. E-mail: shivarajuenvi@gmail.com, anilkumarenvi@jssuni.edu.in; Tel: +91-8277102057
[b] Center for Water, Food and Energy, GREENS TRUST, Turuvekere Taluka, Harikaranahalli, Karnataka, 572215, India
[c] Department of Pharmaceutics, School of Pharmacy, Anurag University, Hyderabad, 500088, Telangana, India
[d] Department of Chemistry, The Oxford College of Engineering, Bengaluru, 560068, Karnataka, India
[e] PG Department of Studies and Research in Environmental Science, Kuvempu University, Shimoga, Karnataka, India
[f] Department of Microbiology, JSS Academy of Higher Education and Research, Mysuru, India
[g] Department of Biotechnology and Bioinformatics, JSS Academy of Higher Education and Research, Mysuru, India
[h] Department of Pharmacognosy, College of Pharmacy, Prince Sattam Bin Abdulaziz University, Alkharj, Saudi Arabia
[i] Department of Pharmacognosy, College of Pharmacy, King Khalid University, Abha, 62529, Saudi Arabia
[j] Institute of Catalysis and Energy Solutions (ICES), College of Science Engineering and Technology, University of South Africa, South Africa
[k] Department of Chemistry, Sri Jayachamarajendra College of Engineering, JSS Science and Technology University, Mysuru, 570 006, India
[l] International Center of Environment and Sustainability (ICESu), JSS Academy of Higher Education and Research, Mysuru, 570015, India

1. Introduction

The environmental concerns and interplay of energy have emerged as paramount challenges hindering the sustainable advancement of the global ecosystem. It is imperative to devise an energy reservoir that is storable, environmentally sustainable, cost-effective, and renewable to address the global energy requisites comprehensively.[1] Hydrogen (H_2) energy emerges as an exemplary primary energy vector for establishing a sustainable future, owing to its renewable nature, storage capability, net-zero emission characteristics, and notably high energy density of 143 KJ g^{-1}, surpassing that of gasoline.[2,3] To date, hydrogen production methods such as steam reforming, methane pyrolysis, ammonia decomposition, and solar thermochemical processes have been explored.[4,5] Despite their potential, these approaches are limited by rigorous reaction conditions, high energy consumption, and challenges in separating byproducts, especially in terms of H_2 storage and transportation.[6] Therefore, extensive investigations have been directed towards the development of alternative hydrogen production methods that meet the increasing global hydrogen demand in an environmentally friendly and cost-effective

manner. In this scenario, photo-electrochemical (PEC) water splitting, utilizing semiconductor materials, remains a subject of global interest due to its ability to directly decompose water into H_2 and O_2 through sunlight absorption. This approach is highly efficient and eco-friendly and holds promise for progress towards a zero-carbon future.[7,8] The PEC water splitting offers a unique advantage over alternative methods due to its capability to produce H_2 and O_2 at distinct electrodes, mitigating issues related to gas mixing and undesirable back reactions. Moreover, the PEC system exhibits lower overpotentials when juxtaposed with electrochemical water splitting. The external voltage allows the mechanism to accelerate the reaction at the required rate by promoting charge separation and migration, resulting in high efficiency.[9] In this context, most research efforts have centred on developing suitable semiconductor materials capable of serving as effective photoelectrodes for green hydrogen fuel generation. Efficient PEC water splitting requires that semiconductors have a minimal band gap of 1.23 eV to maximize light absorption, band edge alignment with water redox potentials, sustained stability, and support for effective charge carrier diffusion[10].[11] Additionally, semiconductor-based photoanodes or photocathodes enable lower operating potentials, facilitating high energy conversion rates in the PEC water splitting, even at low temperatures.

To date, a multitude of photoelectrodes have been explored and optimized for utilization in PEC water splitting, encompassing materials such as TiO_2, Fe_2O_3, ZnO, g-C_3N_4, and WO_3.[12,13] However, limitations such as rapid recombination, susceptibility to photo-corrosion, wide band gaps, low charge carrier mobility, and suboptimal band edge alignment restrict the applicability of these semiconductor materials as photoelectrodes.[14,15] Due to their robustness, versatile composition and structure, strong visible light absorption, and adjustable band properties, perovskite oxides (ABO_3) present an attractive choice for PEC water splitting photoelectrodes.[16] Among the various perovskite oxides, $CeNiO_3$ has emerged as a leading choice in photo-electro-catalysis, characterized by a narrow band gap of 1.51 eV. Its high electrocatalytic efficiency, earth-abundant nature, robust redox cycles, exceptional optical features, environmental sustainability, and the combined effects of photocatalytic and magnetic properties make it highly favourable for hydrogen evolution.[17] Owing to the profusion of oxygen vacancies, CeO_2 metal oxide displays n-type semiconductor properties, with impressive redox reaction capabilities caused by its spatial processes and oxygen-releasing properties.[18–20] Furthermore, the incorporation of ceria (Ce) and nickel (Ni) into the A and B sites of the perovskite framework enhances its electronic and optical characteristics and improves capacitance values while maintaining robust cycling stability. This enhancement is attributed to structural alterations within the ceria crystalline matrix, primarily involving partial replacement of Ce^{4+} ions with Ni^{2+}. The substitution of Ni^{2+} for Ce^{4+} in the $CeNiO_3$ lattice induces structural modifications, which can influence defect formation, the electronic structure, and charge carrier dynamics. Specifically, the incorporation of Ni^{2+} can introduce oxygen vacancies and modify the local coordination environment, enhancing charge separation and transport.[21,22]

Research has consistently revealed that achieving a large surface area and controlling the morphology in catalysts are additional influential factors that highly influence the charge transfer mechanism and light absorption dynamics, contributing to the efficient production of hydrogen and fabrication of highly efficient photoelectrodes, achievable through suitable synthesis methodologies.[23] Various methodologies have been documented for the development of perovskite materials, encompassing techniques such as electrospinning, solvothermal synthesis, co-precipitation, hydrothermal, and sol–gel methods.[24,25] Among these techniques, the sol–gel approach is the most beneficial for the manufacture of $CeNiO_3$ since it is environmentally benign and inexpensive.[26] Ming Yang *et al.* developed a TiO_2@$SrTiO_3$@$BiVO_4$ photoanode for hydrogen evolution, achieving an impressive photocurrent density of 3.7 mA cm^{-2} at 1.23 V *vs.* RHE under AM 1.5 G illumination, along with a peak incident photon-to-current conversion efficiency (IPCE) of 65%.[27] Jin Kim and co-workers investigated PEC water splitting using Fe_3O_4 nanoparticles exsolved in $SrTiO_3$, achieving a photocurrent density of 5.10 mA cm^{-2} at 1.23 V *vs.* RHE, along with excellent durability, maintaining 97% of its initial activity over 24 h.[28] In their study, Ramesh Reddy and colleagues employed 3D ZnO nanostructures for PEC water splitting, achieving a photocurrent density of 0.6 mA cm^{-2} and showing stable performance for up to 5 h under light-on/light-off testing.[29] Xie and colleagues developed a CdS nanosphere photoelectrode for PEC water splitting, achieving a photocurrent density of 5.10 mA cm^{-2} at 1.23 V *vs.* RHE.[30]

According to the available literature, there is a significant gap in research on the implementation of a $CeNiO_3$ perovskite material as a photoelectrode in photoelectrochemical water splitting. This work focuses on cost-effective and stable materials, aligning with sustainable hydrogen production goals, and outlines the synthesis of a $CeNiO_3$ perovskite material utilising a simple, eco-friendly, and economical citrate sol–gel approach. These samples are then explored as photoelectrode materials for generating hydrogen *via* photoelectrochemical water splitting. The manufactured $CeNiO_3$ material was thoroughly characterised using cutting-edge equipment to discover the physicochemical attributes of the resulting material. Additionally, the photo-electro-catalytic performance of the $CeNiO_3$ material has been examined through PEC water-splitting tests. The $CeNiO_3$ material performed well in PEC water splitting, enabling successful generation of sustainable hydrogen fuel.

2. Experiment and methodology

2.1. Materials

Citric acid monohydrate ($C_6H_8O_7{\cdot}H_2O$), cerium nitrate hexahydrate [Ce $(NO_3)_3{\cdot}6H_2O$], nickel nitrate hexahydrate [Ni $(NO_3)_2{\cdot}6H_2O$], ammonia water ($NH_3{\cdot}H_2O$) and other solvents were sourced from Sigma-Aldrich Pvt. Ltd and chosen as precursors for the preparation of $CeNiO_3$ catalysts. Deionized water was

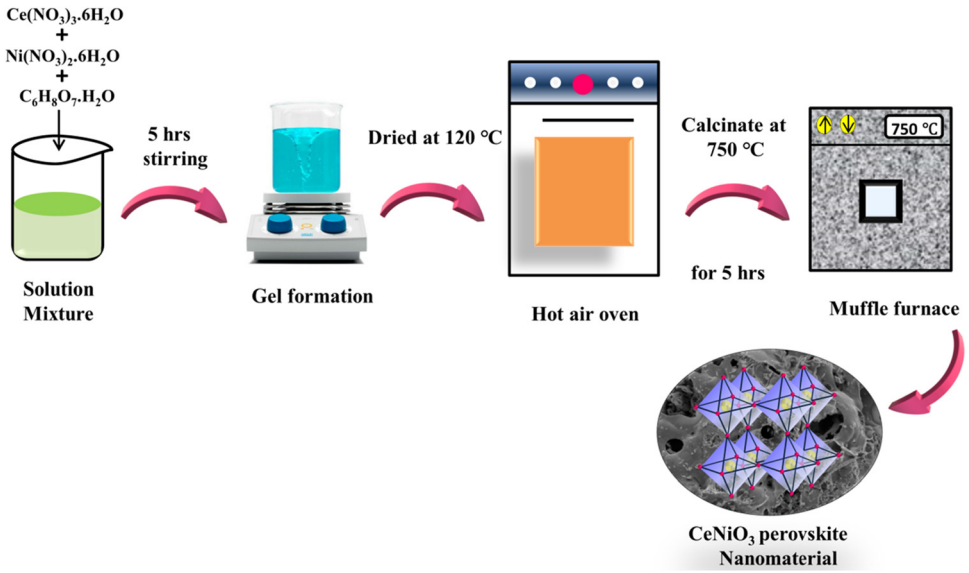

Fig. 1 Visual illustration of the $CeNiO_3$ perovskite material preparation.

employed as the dissolution solvent throughout the experimental process and all the reagents used in this study were of high analytical purity.

2.2. Synthesis of the $CeNiO_3$ catalyst

The $CeNiO_3$ catalytic material was prepared using the universally accepted citrate sol–gel technique and the synthesis techniques employed are depicted in Fig. 1. A stoichiometric volume of cerium nitrate hexahydrate, citric acid monohydrate and nickel nitrate hexahydrate ($Ce : C_6H_8O_7{\cdot}H_2O : Ni = 1 : 3 : 1$) was dissolved in deionized Millipore water (50 mL) and the obtained mixture solution was continuously stirred for 30–35 minutes. The pH value was adjusted between 5 and 6 approximately by adding an ammonia solution sequentially. The above mixture was kept stirring maintaining at a temperature of 90 °C until a green gel formed. The as-obtained homogenized gel was initially dried at 120 °C for 7–10 hours in order to eliminate any remaining nitrates. The ground powder was subjected to calcination at 750 °C for 5 hours to synthesize the target perovskite phase, $CeNiO_3$.

2.3. Fabrication and preparation of the $CeNiO_3$ photoelectrode

A working $CeNiO_3$ photoelectrode was prepared by coating the fabricated photocatalyst as a thin film onto an FTO glass plate. A total of 5 mg of the specimen was thoroughly mixed into 500 mL of Nafion–ethanol during the first 30 minutes of ultrasonication in an effort to create a catalyst-loaded photoelectrode. Thereafter, 20 μL of the suspension was drop cast onto FTO glass measuring 1×1 cm^2 and dried at 150 °C for 3 hours in an oven and later subjected to photoelectrochemical measurement.

2.4. Characterization of $CeNiO_3$

The designed $CeNiO_3$ catalyst underwent a comprehensive array of advanced examinations, delving into its fundamental physicochemical and innate characteristics. Powder X-ray diffraction (XRD) characterization (Shimadzu, Japan) was employed for crystallinity and lattice configuration studies. The photoluminescence (PL) emission was investigated utilizing an FL-1039/40 fluorescence spectrometer (Horiba Jobin Yvon), specifically to examine the charge separation kinetics of the specimen. FTIR was conducted for examination of the vibrational patterns about the stretching and bending modes of the synthesized material (Bruker, ALPHA, 200619, Germany). Field emission scanning electron microscopy (FE-SEM) was carried out using a JEOL-AV JSM-7100F (Singapore) to explore the surface morphology and microstructural features of the $CeNiO_3$ material. Energy-dispersive X-ray (EDX) assessment was carried out to discern the chemical constituents and elemental spatial distribution of the sample employing Super X (JSMIT300, JEOL, Singapore). The elemental composition of the material was elucidated through X-ray photoelectron spectroscopy (XPS) using a PHI 5000 VersaProbe III. The optical attributes of the specimen were assessed utilizing UV-visible absorption spectroscopy using a UV 2600 spectrophotometer (Shimadzu, Japan).

2.5. Photo-electro-chemical characterization

Photo-electro-chemical investigations were conducted utilizing a conventional three-electrode cell configuration (CHI760E) with $CeNiO_3$ photocatalysts serving as the working electrode, where an Ag/AgCl electrode was employed as the reference electrode and a platinum (Pt) rod functioned as the counter electrode. An aqueous solution containing 0.5 M Na_2SO_4 (sodium sulfate) served as the electrolytic medium, maintaining a pH of 5. The photoelectrodes underwent irradiation at an intensity of 100 mW cm^{-2}, employing a 350 W xenon lamp equipped with an AM 1.5G filter. Linear sweep voltammetric (LSV) polarization profiles were acquired within the voltage range of 0 to 1.4 V. The potentials were referenced to the

reversible hydrogen electrode (RHE) by applying the equation $E_{RHE} = E_{Ag/AgCl} + E^{0}_{Ag/AgCl} + 0.059 * pH$. Mott–Schottky curves were generated under illumination conditions at a frequency of 1000 Hz. Electrochemical impedance spectroscopy (EIS) was explored across a frequency range of 1 to 100 kHz. The electrodes underwent durability examination *via* chronoamperometric (CA) studies.

3. Results and discussion

3.1. XRD analysis

XRD assessment was conducted on perovskite $CeNiO_3$ particles to discover their crystalline structure and phase purity. The outcomes are depicted in Fig. 2. XRD analysis of the pristine $CeNiO_3$ catalyst has elucidated the presence of an orthorhombic phase. The XRD pattern exhibited distinct *d* peaks at 2θ angles of 28.45°, 33.08°, 37.16°, 43.16°, 47.48°, 56.34°, 59.12°, 62.92°, 69.51°, 76.75°, and 79.20°, which are attributed to the lattice planes of (111), (002), (112), (221), (040), (321), (123), (331), (242), (412), and (161), respectively, indicating the crystallinity of the $CeNiO_3$ sample. These outcomes match well with the reference data (ID number: mp-776207) and previously stated research work.[21] The peaks perceived at 33.08°, 47.48°, 59.12°, 69.51°, 76.75°, and 79.20° correlate to the (002), (040), (123), (242), (412) and (161) crystallographic planes of cerium dioxide (CeO_2), as indicated by JCPDS No: 81-0792. The XRD pattern of cubic NiO exhibits strong signals at 2θ angles of 37.16°, 43.16°, and 62.92° analogous to the crystallographic planes (112), (221), and (331) respectively, as designated by JCPDS No: 75-0197.[31] The XRD pattern, showing no additional diffraction peaks, supports the excellent crystallinity and phase homogeneity of the synthesized material.

3.2. FE-SEM analysis

The surface morphologies of as-prepared $CeNiO_3$ perovskite materials are scrutinized through the utilization of FE-SEM.

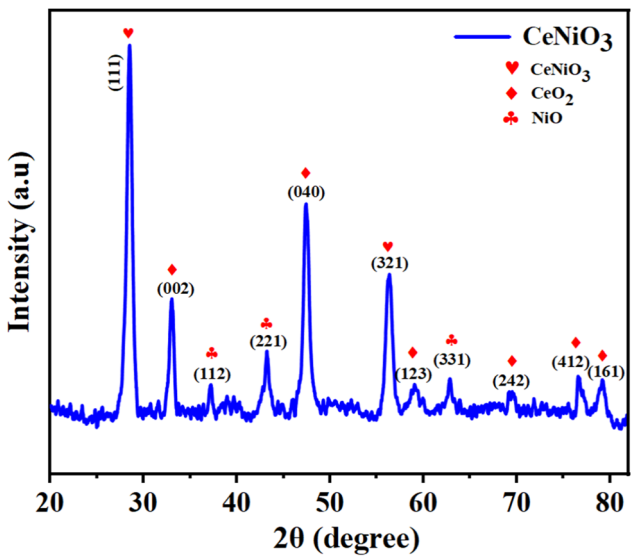

Fig. 2 XRD spectrum of the $CeNiO_3$ perovskite photocatalyst.

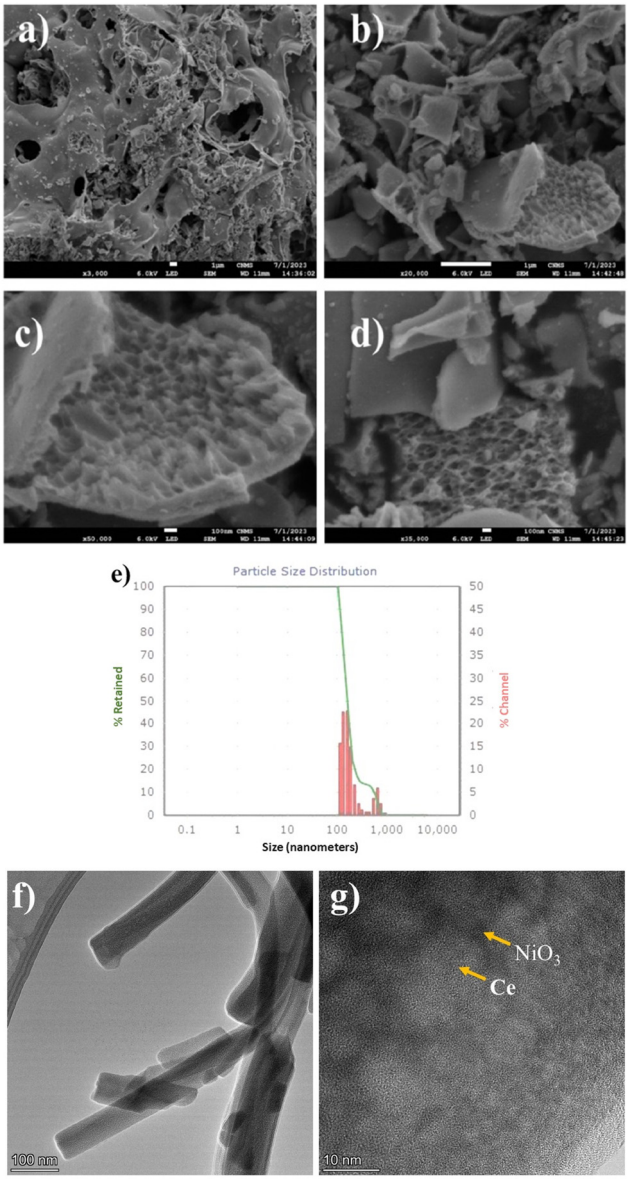

Fig. 3 (a)–(d) FE-SEM micrographs, (e) DLS results of the $CeNiO_3$ perovskite photocatalyst and (f) and (g) TEM images.

Fig. 3 shows a surface morphology micrograph depicting the synthesized $CeNiO_3$ material. These FESEM photographs indicate the formation of the $CeNiO_3$ material with rough surface morphology. FESEM pictures of $CeNiO_3$ unveiled a myriad of irregularly shaped pores exhibiting varying diameters and the material showcased a notably elevated surface area, highlighting its potential for enhanced catalytic activity. The porous architecture inherent in the $CeNiO_3$ material is widely recognized for its capacity to improve the photo adsorption performance, specifically in the segregation of electron–hole pairs.[32,33]

3.3 TEM analysis

The rod-like shape of the synthesised $CeNiO_3$ nanostructures with uniform dimensions and smooth surfaces is clearly visible

in the TEM image (Fig. 3(f)), indicating that a well-defined crystalline phase was successfully formed. Effective oversight throughout the synthesis process is suggested by the nanorods' apparent well-dispersed state and lack of noticeable aggregation. The high crystallinity and purity of the prepared material are confirmed by the uniform contrast and distinct edges that were observed.

Additionally, the lattice structure and elemental dispersion within the $CeNiO_3$ matrix can be obtained from the image (Fig. 3(g)). The successful integration of Ni into the Ce lattice structure is confirmed by the distinct lattice fringes that match the interplanar spacings of the Ce and NiO_3 phases. Good crystallinity and close contact between the Ce and NiO_3 domains are indicated by the presence of clearly resolved fringes, which can promote effective charge transfer across the interface. These structural characteristics are anticipated to foster synergistic interactions between Ce and Ni species, improving the $CeNiO_3$ nanocomposite's catalytic and electrochemical performance.[34]

3.4. EDX analysis

EDX analysis was conducted to scrutinize the degree of purity, elemental composition and distribution within the 100–300 nm range of the fabricated $CeNiO_3$ photocatalyst. Fig. 4(a) depicts the obtained EDX outcomes. The EDX assessment verifies the existence of ceria (Ce), nickel (Ni), and oxygen (O) within the sample, providing substantial evidence for the successful formation of the $CeNiO_3$ photocatalyst. The exceptional purity of the $CeNiO_3$ structures synthesized *via* sol–gel methodologies was substantiated by the absence of discernible intense peaks corresponding to any additional constituents or impurities within the materials. DLS results of the $CeNiO_3$ perovskite photocatalyst indicated that the particle size distribution varied in the 100–220 nm range (Fig. 3(e)). Additionally, the elemental mapping evaluation depicted in Fig. 4(b)–(e) revealed a spectrum comprising three different components, delineating the existence of Ce (red), Ni (blue), and O (yellow).

3.5. XPS analysis

XPS has been applied to evaluate the chemical states and elemental constituents of the $CeNiO_3$ perovskite photocatalyst. Fig. 5(a) confirms the homogeneity of the $CeNiO_3$ material, as evidenced by the observation of Ce 3d, Ni 2p, and O 1s signals, with no additional elemental constituents detected during the FE-SEM and EDX analyses. The determination of the binding energy of oxygen atoms provides insights into the oxygen's chemical state and enables the identification of oxygen vacancies that are induced within the material's crystalline lattice. The metal cations located at either the A-site or the B-site in the perovskite structure demonstrate ratios of A^{n+1}/A^n and B^{n+1}/B^n, respectively, showcasing their catalytic redox potential.[35] The Ce 3d spectrum prominently manifests distinct peaks corresponding to Ce^{3+} $3d_{3/2}$ and Ce^{4+} $3d_{5/2}$ electron orbitals, along with the observable satellite signals (Fig. 5(b)). Binding energies for Ce^{3+} $3d_{3/2}$ are well recorded at 916.98 eV, 905.39 eV, and 900.15 eV. Ce^{4+} $3d_{5/2}$ demonstrates distinctive binding energies

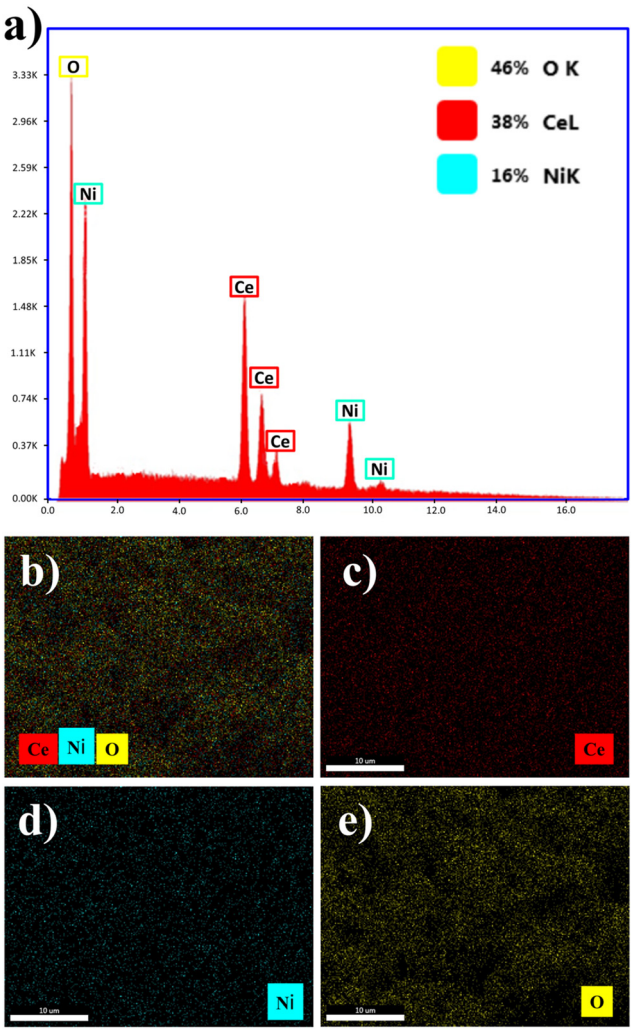

Fig. 4 (a). EDX profiles of the $CeNiO_3$ specimen and (b)–(e) elemental mapping analysis of the $CeNiO_3$ perovskite photocatalyst.

at 897.53 eV, 888.48 eV, and 882.77 eV, respectively.[36] Fig. 5(c) illustrates the Ni 2p XPS patterns, revealing spin–orbit doublets of Ni $2p_{3/2}$ and Ni $2p_{1/2}$ at 855.19 eV and 872.98 eV respectively. Additionally, there are two observable satellite spikes positioned at 861.12 eV and 883.53 eV. The dual peaks observed in the Ni 2p spectrum, positioned at 855.19 eV and 861.12 eV, are attributed to the Ni^{3+} oxidation state. Concurrently, the spikes positioned at 883.53 eV and 872.98 eV are assigned to the Ni^{2+} states.[37,38] The binding energies observed in the O 1s XPS spectra, specifically the oxygen vacancies (O_v) at 531.33 eV and lattice oxygen (O_L) at 528.91 eV, as demonstrated in Fig. 5(d), serve as conclusive evidence of the existence of O_2^- species within the crystalline framework of the $CeNiO_3$ material.[39] Higher levels of oxygen vacancies facilitate rapid ionic diffusion during the charge transfer mechanism. The XPS outcomes illustrate that the $CeNiO_3$ material exhibits advantageous characteristics associated with two redox pairs (Ce^{3+}/Ce^{4+} and Ni^{2+}/Ni^{3+}), along with the presence of oxygen vacancies within its structural framework. These attributes contribute to an enhanced capacity for charge storage at a rapid rate.

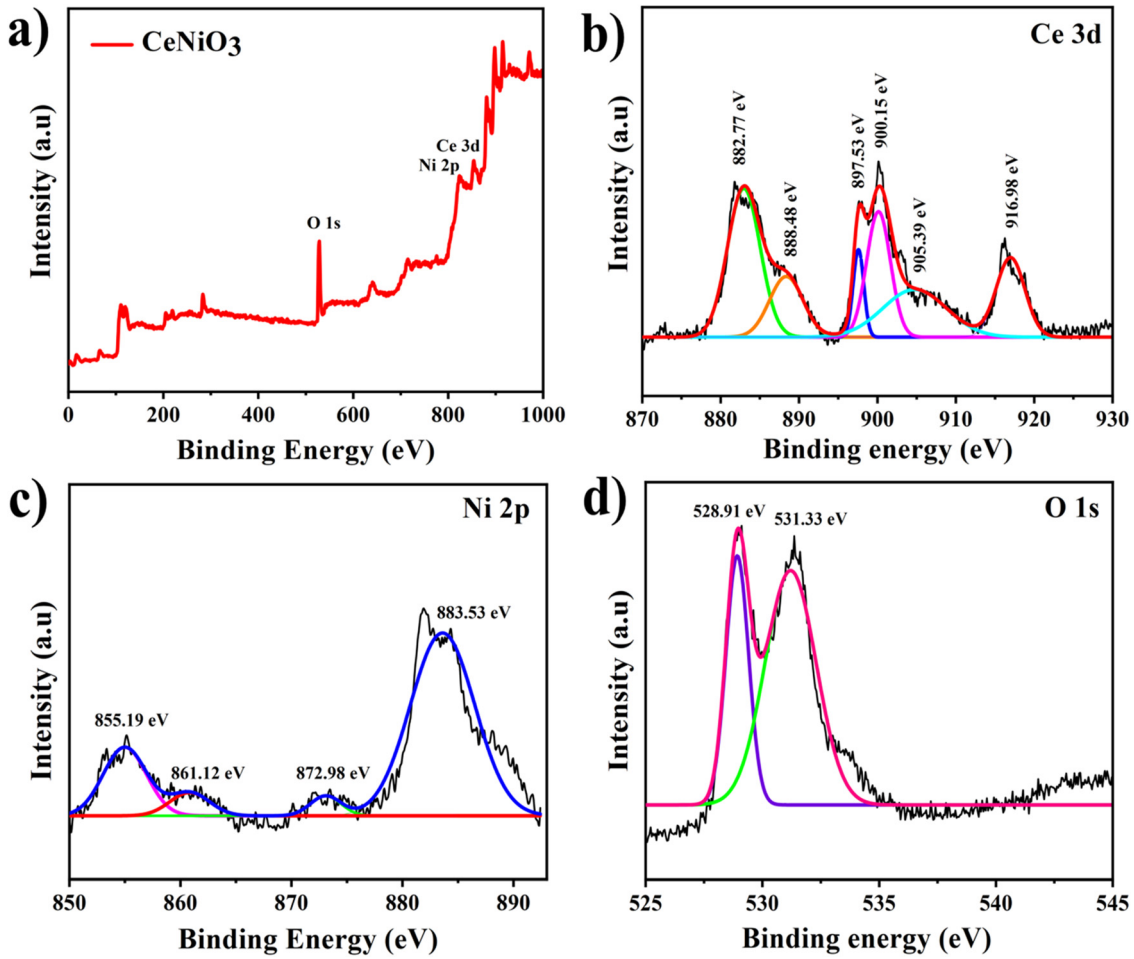

Fig. 5 (a). XPS full scan spectra of the $CeNiO_3$ material, (b) Ce 3d, (c) Ni 2p, and (d) O 1s.

3.6. UV-vis spectra

Band-gap energy and the light-scattering characteristics of the manufactured specimen were evaluated using UV-visible spectroscopy. Fig. 6(a) and (b) illustrate the UV-visible spectroscopic data, as well as the corresponding Tauc plot for the given experimental conditions. The $CeNiO_3$ sample shows a red shift in its absorption onset, broadening into the visible light region, which enhances visible light absorption.[40] The

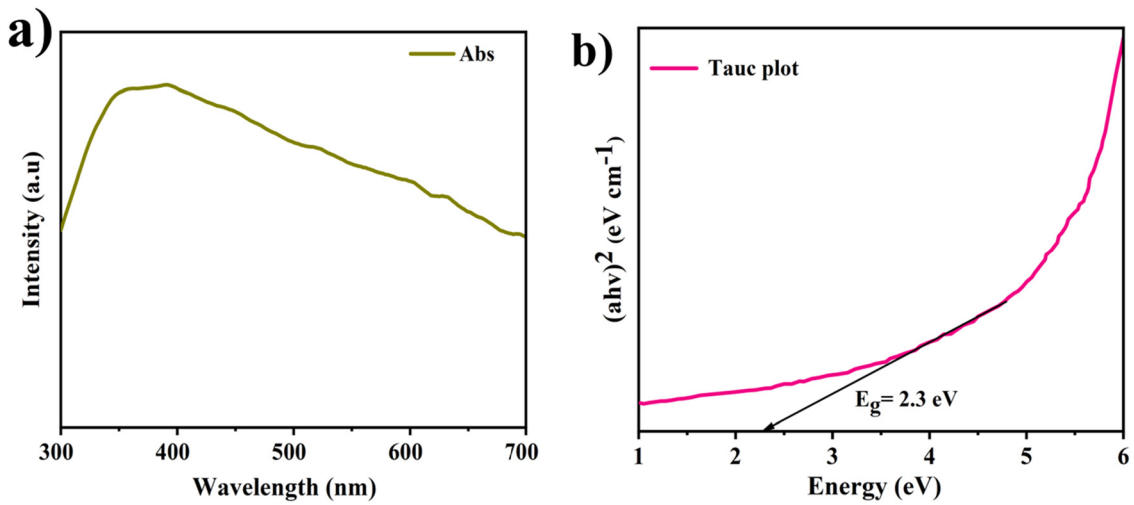

Fig. 6 (a) UV-visible absorbance spectra of the $CeNiO_3$ perovskite photocatalyst. (b) Calculated Tauc plot graph of the $CeNiO_3$ perovskite photocatalyst.

band-gap energy (E_g) of the fabricated $CeNiO_3$ specimen was determined employing Tauc's equation (eqn (1)), and the outcomes are presented in Fig. 6(b).

$$(\alpha h\nu)^2 = A(h\nu - E_g) \quad (1)$$

The $CeNiO_3$ catalyst exhibited E_g = 2.3 eV, which implies that the material possesses advantageous optical characteristics, rendering it well-suited for engaging in photo-electro-catalytic applications using visible light.

Theoretical computation of the semiconductor's VB and conduction band CB potentials can be achieved by applying the Mulliken electronegativity and the semiconductor's band-gap through the subsequent formula.[41]

$$E_{VB} = X - E_e + 0.5E_g \quad (2)$$

$$E_{CB} = E_{VB} - E_g \quad (3)$$

where E_{VB} and E_{CB} symbolize the VB and CB potentials, respectively, E_g represents the band gap energy (2.3 eV), and E_e signifies the energy level of free electrons calibrated on the hydrogen scale, maintaining a constant value of 4.5 eV. Furthermore, X stands as the absolute electronegativity value of $CeNiO_3$.[42] The detailed calculation of the conduction band and valence band of the $CeNiO_3$ material is as follows:

The first ionization energy of the cerium element (Ce):
I_1 = 534.4 kJ mol^{-1}

The first electron affinity of the cerium element (Ce):
E_1 = 50 kJ mol^{-1}

The absolute electronegativity of the cerium element (Ce):

$$X = \frac{1}{2}(I_1 + E_1) = \frac{1}{2}(534.4 + 50) = 292.2 \text{ kJ mol}^{-1}$$

Converting into eV,

$$\frac{292.2}{96.48} = 3.02 \text{ eV}$$

For nickel (Ni): I_1 = 737.1 kJ mol^{-1} and E_1 = 111.65 kJ mol^{-1}; therfore,

$$X = \frac{1}{2}(I_1 + E_1) = \frac{1}{2}(737.1 + 111.65) = 424.37 \text{ kJ mol}^{-1}$$

Converting into eV,

$$\frac{424.37}{96.48} = 4.39 \text{ eV}$$

For oxygen (O): I_1 = 1313.9 kJ mol^{-1} and E_1 = 140.97 kJ mol^{-1}; therfore,

$$X = \frac{1}{2}(I_1 + E_1) = \frac{1}{2}(1313.9 + 140.97) = 727.43 \text{ kJ mol}^{-1}$$

Converting into eV,

$$\frac{727.43}{96.48} = 7.53 \text{ eV}$$

The geometric mean of the absolute electronegativity for $CeNiO_3$ is calculated as follows:

$$X = \sqrt[5]{3.02 \times 4.39 \times 7.53^3} = 5.63 \text{ eV}$$

The band gap of $CeNiO_3$ was obtained by the UV-vis measurements and determined to be 2.3 eV (Fig. 6b).

Therefore, the valence band of $CeNiO_3$ is calculated as follows:

$$\begin{aligned} E_{VB} &= X - E_e + 0.5E_g \\ &= 5.63 - 4.5 + 0.5 \times 2.3 \\ &= 2.28 \text{ eV} \end{aligned}$$

The conduction band of $CeNiO_3$ is calculated as follows:

$$\begin{aligned} E_{CB} &= E_{VB} - E_g \\ &= 2.28 - 2.3 \\ &= -0.02 \text{ eV} \end{aligned}$$

The computed E_{VB} value for $CeNiO_3$ is 2.28 eV, while its corresponding E_{CB} value is −0.02 eV.

3.7. FTIR spectra

The functional groups and discernible chemical bonds of the synthesised $CeNiO_3$ catalyst specimens were assessed using FTIR, and the findings are illustrated in Fig. 7(a). The fabricated specimen displayed stretching vibrations originating from crystallized water (–OH) molecules, potentially contributing to the broad transmission detected at 3440.01 cm^{-1} and 1773.46 cm^{-1}. The Ni^{2+}/Ni^{3+} cations, resembling the asymmetric sharp bands, were detected in the $CeNiO_3$ sample within the spectral range of 1374.37 cm^{-1} to 1633.85 cm^{-1}. The transmittance bands detected at 707.12 cm^{-1} are credited to the stretching of Ni–O bonds. Two discrete peaks identified at 1036.01 and 505.20 cm^{-1} are correlated with Ce–O stretching vibrations.[21]

3.8. PL analysis

To comprehend the segregation of the charges generated by light exposure during the PEC process, photoluminescence studies were performed at an excitation wavelength of 365 nm at ambient temperature. Fig. 7(b) displays the emission spectra of the $CeNiO_3$ specimen. Generally, a decrease in PL emission intensity indicates high charge carrier separation efficacy, ultimately optimizing the photo-electro-catalytic performance of photocatalysts. The PL spectra of the $CeNiO_3$ material disclosed dual peaks, with a lower ultraviolet-excitonic band at 412 nm and a higher green emission band at 468 nm. The UV-excitonic region is designated for charge

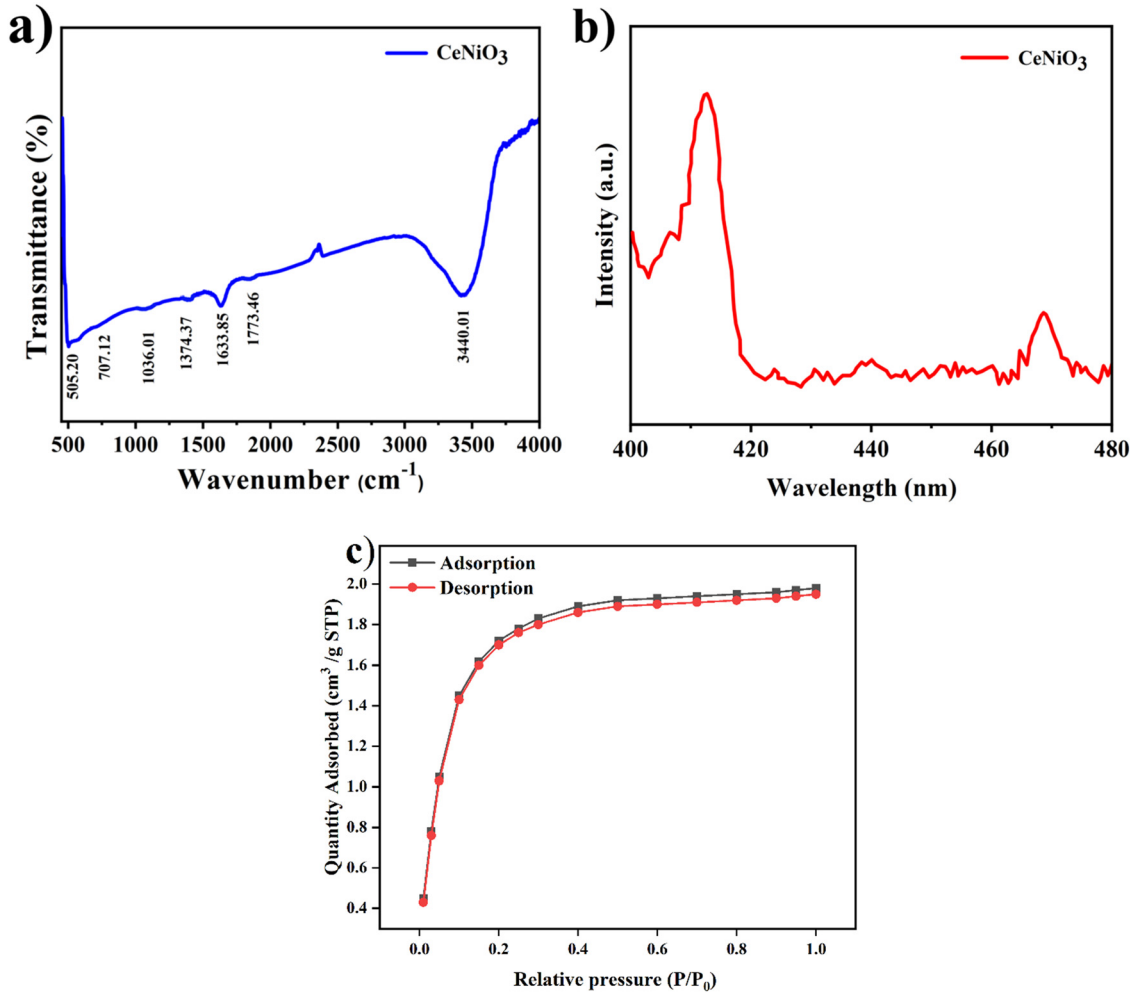

Fig. 7 (a) FTIR spectra, (b) PL spectra of the $CeNiO_3$ perovskite photocatalyst and (c) BET isotherm.

carrier recombination, while the green emission region is attributed to the occurrence of oxygen vacancies.[43] The PL spectra of $CeNiO_3$ exhibited a considerable decline in intensity, suggesting enhanced effectiveness in transferring and separating electron and hole pairs.[44]

3.9. BET isotherm

According to IUPAC classification, the nitrogen adsorption–desorption isotherm of $CeNiO_3$ (Fig. 7(c)) displays a Type I(a) profile, signifying a microporous structure. Adsorption inside micropores is confirmed by a plateau after a sharp uptake at a low relative pressure ($P/P_0 < 0.1$). With a pore volume of 0.00414 $cm^3\ g^{-1}$ and an average pore diameter of 0.9 nm, the BET surface area was found to be 18.4 $m^2\ g^{-1}$. These values correspond to the development of a dense perovskite framework and tiny micropores. The compact configuration of metal–oxygen octahedra results in the low surface area and pore volume that are characteristic of perovskite oxides. Strong reactant interactions and effective charge transfer in catalytic or electrochemical processes can be facilitated by the confined micropores, even due to their limited porosity.

3.10. Photo-electro-chemical measurements

To interrogate the photo-electro-chemical performance of the $CeNiO_3$ perovskite photocatalyst, a three-electrode configuration was employed within a 0.5 M Na_2SO_4 electrolytic medium. Linear sweep voltammogram patterns of the $CeNiO_3$ photoelectrode are illustrated in Fig. 8(a). Under dark conditions, the current density remains minimal. However, upon exposure to solar radiation, a significant augmentation in current density is observed. The elevated photocurrent density signifies the effective sensitivity of the photoelectrode materials to the solar spectrum. This pronounced generation of photocurrent signifies that the semiconductor material possesses a high degree of photoactivity.[4] The resulting photocurrent densities recorded for $CeNiO_3$ were established to be 15.14 mA cm^{-2} and 5.1 mA cm^{-2} with the influence of light and in dark mode at the specific potential of 1.4 V *vs.* the RHE. The exceptional functionality of $CeNiO_3$ stems from its uniform topological characteristics, porous nature, high surface area, and electronic structure, substantially enhancing the higher light absorption with efficient charge transformation within the semiconductor material.[45]

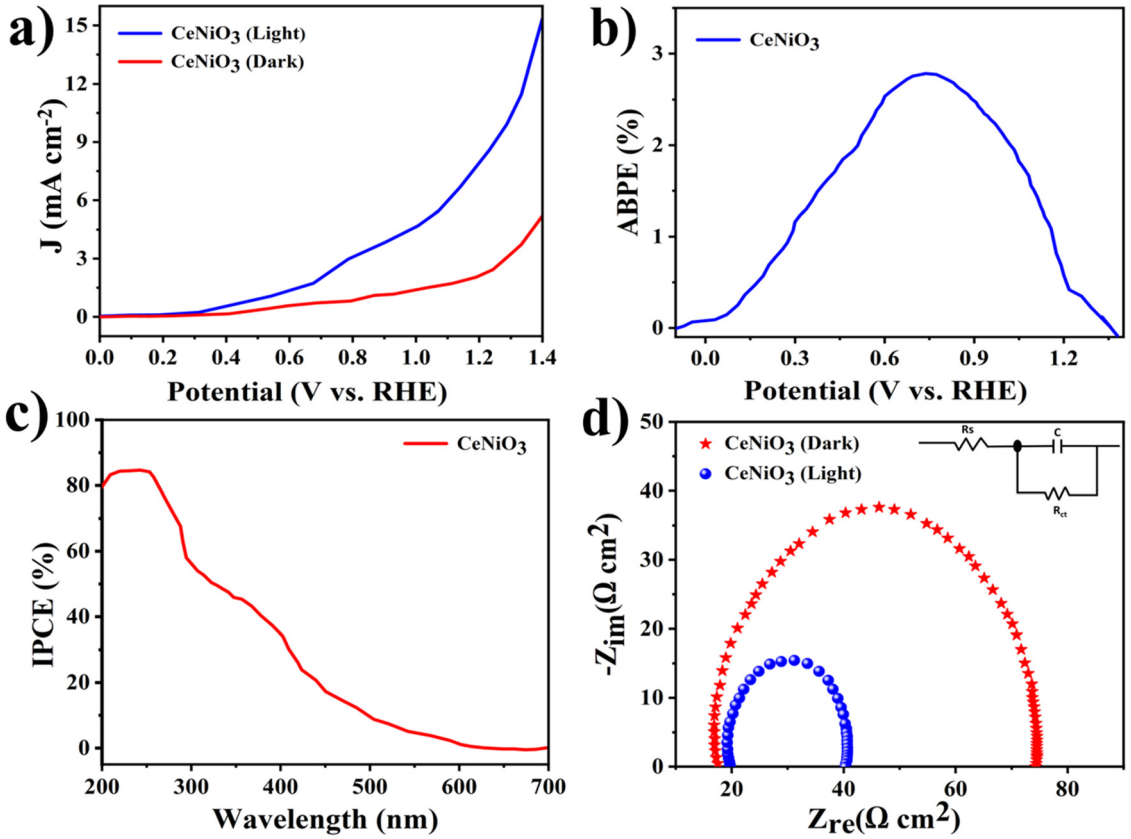

Fig. 8 (a) LSV curves, (b) (ABPE%) plot, (c) (IPCE%) graph, and (d) EIS Nyquist plot of the $CeNiO_3$ electrode (the inset shows an equivalent circuit model).

Furthermore, achieving elevated photocurrent density under minimal applied bias poses a pivotal obstacle in improving the efficacy of water-splitting approaches. Solar-to-hydrogen (STH) conversion efficiencies (η) of the photoelectrode under the influence of an external bias potential against the RHE have been assessed using the following equation:

$$\eta = \frac{J \times (1.23 \times V_b)}{P_{light}} \times 100\% \quad (4)$$

In this equation, J stands for the photocurrent density, and 1.23 V corresponds to the equilibrium potential that is required for splitting water into O_2 and H_2. V_b is the applied bias with respect to P_{light}, which is the power density of incident light, and RHE. Fig. 8(b) presents a plot of photoconversion efficiency (η%). The highest efficiency achieved for $CeNiO_3$ was 2.76%, reflecting its impressive ability to convert incident light into hydrogen fuel.

Additionally, the assessment of incident photon to current conversion efficiency (IPCE) is undertaken to precisely estimate the photoelectric conversion efficacy of the photoelectrode across a spectrum of incident light wavelengths, utilizing the subsequent formula.

$$\text{IPCE } (\%) = \frac{J \times 1240}{\lambda \times P_{light}} \times 100\% \quad (5)$$

In this study, the photocurrent density is expressed by the variable J, the value of 1240 is a product of the speed of light, P_{light} depicts the luminous power density, and λ indicates the incident wavelength. As presented in Fig. 8(c), a high IPCE of 80.10% is demonstrated by the $CeNiO_3$ photoelectrode over the 300–700 nm light spectrum. $CeNiO_3$ demonstrates heightened photoresponsivity, potentially attributed to the provision of additional reactive sites and efficient pathways for charge carrier transmission, facilitating light capture and electron excitation.[46]

EIS is a method for elucidating the dynamics of charge carrier migration and assessing interfacial charge transfer resistance (R_{ct}). Fig. 8(d) showcases the intriguing findings from the EIS analysis conducted on the $CeNiO_3$ photoelectrode under both dark and illuminated conditions. The simulated circuit model representing the charge transfer mechanisms within photocatalysts is depicted in the inset of Fig. 8(d). The radius of the Nyquist arc collected in EIS is intricately linked to the kinetics of the photo-electro-catalytic reaction occurring on the surface of the photoelectrode. It quantifies the impedance to charge transfer at the photoelectrode–electrolyte interface. A smaller arc diameter signals higher electron transportation, which supports better segregation of light-induced charge carriers, thereby enhancing the proficiency of PEC water splitting.[47] The R_{ct} value for the $CeNiO_3$ photoelectrode is listed in Table 1. EIS spectra (Fig. 8(d)) of $CeNiO_3$ unveil that, in

Table 1 EIS fitting results for the $CeNiO_3$ photoelectrode

Sample	Condition	(R_{ct}) (Ω cm^2)
$CeNiO_3$ photoelectrode	Dark	56.94
$CeNiO_3$ photoelectrode	Light	20.13

comparison with the dark mode, a smaller semicircle is noticed under irradiation, signifying faster charge carrier mobility due to its highly porous nature and dual-metal synergy observed in the $CeNiO_3$ photoelectrode in the Na_2SO_4 electrolyte. Notably, there is remarkable inhibition of the charge carrier recombination.[48,49]

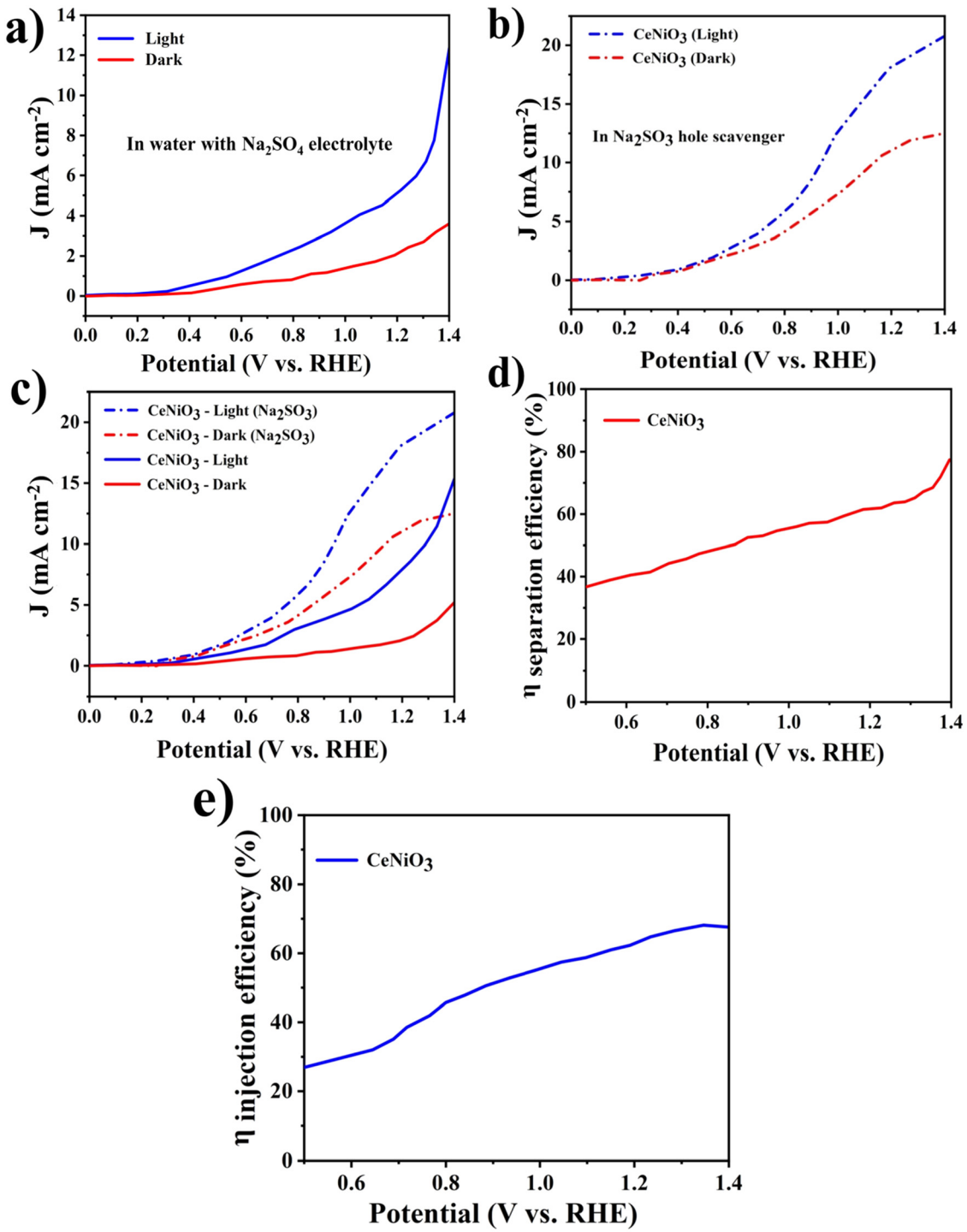

Fig. 9 (a) LSV curves with 0.5 M Na_2SO_4 electrolyte in water, (b) and (c) with addition of 0.5 M Na_2SO_3 solution for sulfite oxidation as a hole scavenger, (d) charge separation efficiency of the $CeNiO_3$ photoelectrode, and (e) charge injection efficiency of the $CeNiO_3$ photoelectrode.

To provide insight into the catalytic process, comprehensive evaluation of carrier kinetics is systematically performed. The charge separation efficiency ($\eta_{separation}$) and charge injection efficiency ($\eta_{injection}$) of the $CeNiO_3$ photoelectrode were assessed employing 0.5 M Na_2SO_3 as a hole scavenger with Na_2SO_4 electrolyte, as depicted in Fig. 9(a)–(c), applying the following equation:

$$\eta_{separation} = \frac{J_{H_2O}}{J_{Na_2SO_3}} \quad (6)$$

$$\eta_{injection} = \frac{J_{Na_2SO_3}}{J_{abs}} \quad (7)$$

where J_{H_2O} and $J_{Na_2SO_3}$ stand for the photocurrent densities acquired for water oxidation and sulfite oxidation, and J_{abs} denotes the photo-current density achieved at 100% internal quantum efficiency, respectively. $\eta_{separation}$ quantifies the efficacy of separating photo-induced charge carriers to yield holes that reach the surface. $\eta_{injection}$ signifies the fraction of holes efficiently delivered into the water for oxidation. As shown in Fig. 9(d) and (e), the $CeNiO_3$ photoelectrode delivers the maximum $\eta_{separation}$ efficiency and $\eta_{injection}$ efficiency of 77% and 67% at 1.4 V *vs.* RHE. The favourable band structure, carrier transport properties, surface attributes, electronic characteristics and catalytic performance of the $CeNiO_3$ photoelectrode synergistically contribute to its remarkable efficiency in charge separation and injection processes.[50,51]

Mott–Schottky (M–S) analysis was employed to derive the flat band potential (V_{fb}) of the $CeNiO_3$ material, aiding in the elucidation of its charge transfer dynamics. The following Mott–Schottky equation is exploited to derive the flat-band potential (V_{fb}).

$$\frac{1}{C^2} = \frac{2}{e\varepsilon\varepsilon_0 N_d}\left[(V - V_{fb}) - \frac{kT}{e}\right] \quad (8)$$

where C denotes the capacitance due to space charge, e represents the elementary charge, ε stands for the dielectric constant, k and T represent the Boltzmann constant and temperature, N_d indicates the charge carrier density, V_{fb} signifies the flat band potential, and ε_0 symbolizes the permittivity of free space Fig. 10(a) shows the M–S graph. The V_{fb} can be extrapolated using the X-intercept from the M–S plot. The verified V_{fb} value for the $CeNiO_3$ sample is recorded as 0.31 V. The reduced V_{fb} observed for $CeNiO_3$ suggests a diminished onset potential when exposed to light. The upward shift in the $CeNiO_3$ electrode signifies a lowering in band bending, which promotes the transfer of electrons.[52]

In order to ensure scalable and reliable hydrogen production, the enduring stability of the photoanode is crucial. Long-term stability of the $CeNiO_3$ photoelectrode's photocurrent was investigated through chronoamperometric analysis. During these experiments, the photoanodes underwent continuous exposure to irradiation as presented in Fig. 10(b). The $CeNiO_3$ photoelectrodes demonstrated sustained and durable J (mA cm^{-2}) of 11.17 mA cm^{-2} at 0.8 V *vs.* RHE, with minimal decline in density of current observed over an extended period. Even after 10 hours of testing, the photocurrent density remains stable, demonstrating the photoelectrode's remarkable resilience against photo-induced corrosion.[53] These findings underscore the photocatalyst's durability under light exposure, validating its potential for efficient use in a photoelectrochemical water-splitting system. The PEC water-splitting performance of the $CeNiO_3$ photoelectrode was compared with that of previously reported materials, as outlined in Table 2.

The stability of the catalyst during the photoreaction was further evaluated by analyzing the XRD pattern of the used $CeNiO_3$ sample (Fig. 11(a)). No significant changes were observed in the diffraction peaks, confirming that the crystal structure of $CeNiO_3$ remained intact after the photoelectrocatalytic reaction. This indicates the excellent structural stability and reusability of the synthesized catalyst for practical hydrogen generation and degradation applications. The post-reaction SEM image of the $CeNiO_3$ sample is displayed in Fig. 11(b). After the hydrogen evolution process, the morphology almost

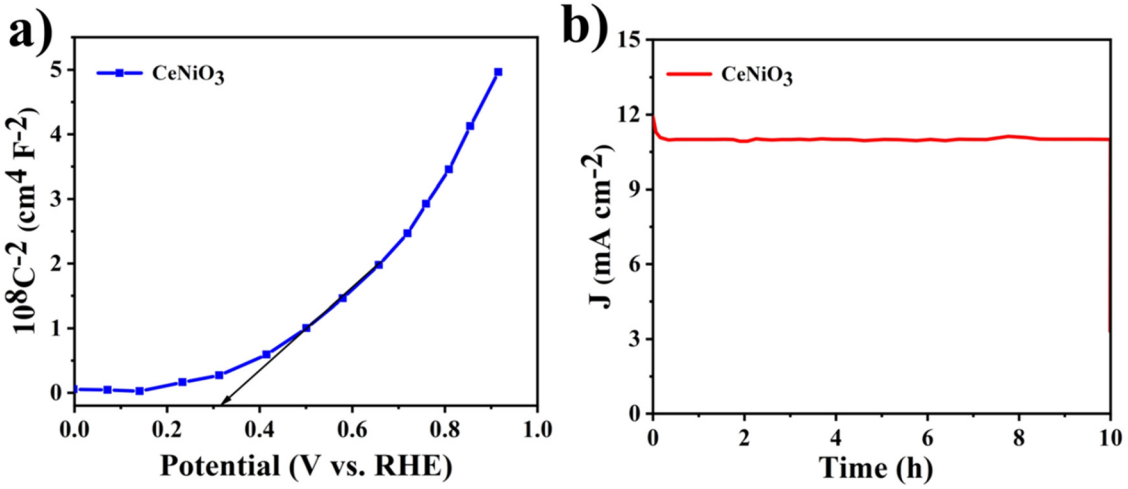

Fig. 10 (a) M–S plot and (b) stability measurements of the $CeNiO_3$ photoelectrode.

Table 2 A comparative analysis of the PEC efficiency of the $CeNiO_3$ perovskite against other materials

Materials	Conditions	J (mA cm^{-2}) (V *vs.* RHE)	Ref.
$CeNiO_3$	0.5 M Na_2SO_4	15.14 at 1.4	Present work
CdS	0.1 M Na_2SO_3	5.10 at 1.23	30
O_3/W	0.5 M H_2SO_4	1.71 at 1.23	54
TiO_2/$BiVO_4$	0.1 M KOH	1.5 at 1.23	55
ZnO	0.25 M KOH	0.6 at 2.4	29

remains the same, suggesting that the catalyst's structural integrity is well maintained. The absence of any apparent particle fusion or agglomeration indicates that the $CeNiO_3$ surface has maintained its dispersed state. Under reaction conditions, the irregularly aggregated and flake-like particles remain distinct and exhibit good morphological stability and resistance to irradiation. The XPS spectra (Fig. 11(c)) show no noticeable shift or change in peak intensities or binding energy positions upon post-analysis, suggesting that the oxidation states of Ce, Ni, and O do not significantly alter following reaction. This confirms the structural integrity and chemical stability of $CeNiO_3$ by indicating that its surface composition and chemical environment are stable and that there has not been a noticeable shift in the electronic structure.

3.11. Detailed reaction mechanism of water splitting in PEC systems

The mechanism by which $CeNiO_3$ enables water splitting encompasses a series of steps that leverage sunlight to yield H_2 and O_2. As illustrated in Fig. 12, this process begins with $CeNiO_3$ absorbing photons, leading to electron–hole pair creation. These charge carriers engage in redox reactions with water adsorbed on the $CeNiO_3$ surface, where holes oxidize water to release O_2, and electrons reduce protons to form H_2. $CeNiO_3$'s structure aids in efficient charge separation, positioning it as a key material in solar-driven hydrogen production. The reactions at both electrodes are summarized here.

$$2h^+ + H_2O \rightarrow \frac{1}{2}O_2 + 2H^+ \quad \text{(Oxidation reaction)} \tag{9}$$

$$2e^- + 2H^+ \rightarrow H_2 \text{ (Reduction reaction)} \tag{10}$$

$$2H_2O \rightarrow 2H_2 + O_2 \text{ (Overall water splitting)} \tag{11}$$

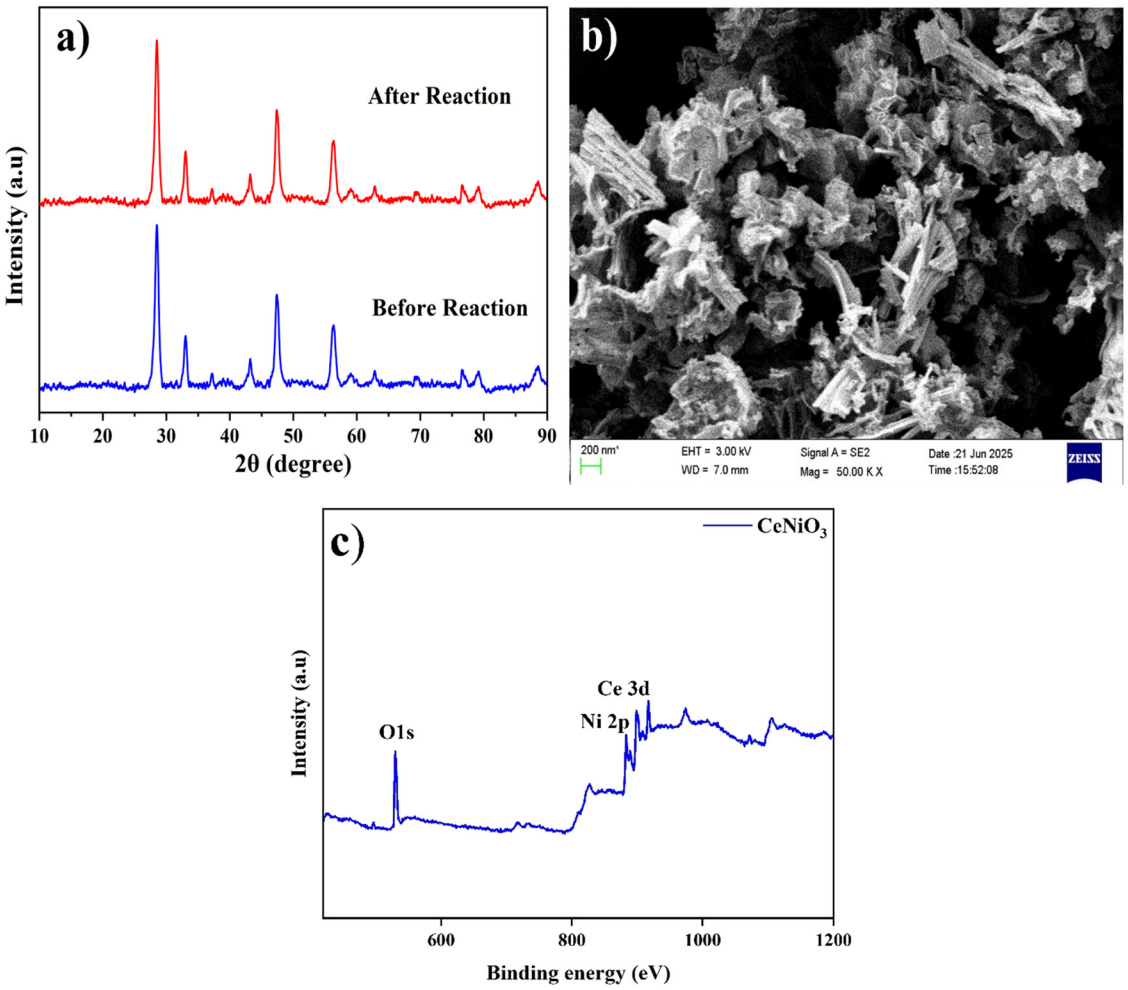

Fig. 11 Post analysis of $CeNiO_3$: (a) XRD, (b) SEM and (c) XPS.

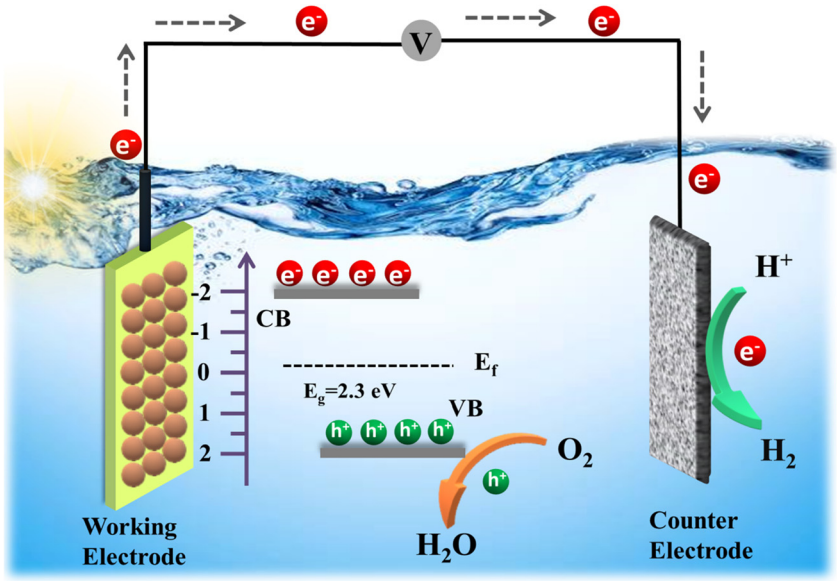

Fig. 12 Visual depiction of the PEC water splitting mechanism over the $CeNiO_3$ photoelectrode.

4. Conclusion

To summarize, this work presents the fabrication of $CeNiO_3$ perovskite structures using a citrate sol–gel technique, specifically designed for an enhanced hydrogen evolution reaction under a visible light driven PEC based water splitting process. Comprehensive analyses were performed on the material to investigate its crystalline arrangement, morphological features, elemental makeup, and optical properties. These assessments conclusively validated the fabrication of the $CeNiO_3$ perovskite with the targeted structural and chemical attributes. XRD scans confirmed the orthorhombic phase in $CeNiO_3$ and FE-SEM photographs of the specimen uncovered an uneven, porous structure. The $CeNiO_3$ photocatalyst displayed a narrow band-gap of 2.3 eV, emerging as an ideal candidate for harnessing the power of visible light irradiation. Moreover, the VB and CB potentials of the $CeNiO_3$ material are calculated to be 2.28 and −0.02 eV, respectively. $CeNiO_3$ has been deployed as a photoelectrode for PEC measurements under illumination. The cerium nickel oxide photoelectrode exhibits outstanding PEC activity, with a current density of 15.14 mA cm^{-2} recorded at 1.4 V and an ABPE% of 2.76%. Remarkably, the $CeNiO_3$ electrode demonstrates exceptional photoelectrochemical stability over a prolonged duration, with negligible photocurrent density deterioration. The aforementioned results illustrate the immense potential of $CeNiO_3$ as a stable and efficient photoelectrode material for hydrogen generation. Future objectives may entail further optimisation of synthetic parameters, exploration of $CeNiO_3$-based tandem PEC systems, and implementation into practical devices for real-world uses, thus promoting the shift towards a carbon-neutral energy economy.

Author contributions

Anusha Hosakote Shankara: examination; data organization, systematic/theoretical analysis, conception, and writing – initial draft. Vinod Divya: visualization and review & editing. V. Rajeshwar, Usha Jinendra, Jagadeep Chandra S, Elayaperumal Sumitha, Basavarajappa Sannappa Hanumanthappa, Kotermane Mallikarjunappa Anilkumar, Peter R. Makgwane, and Honnegowdanahalli Shivabasappa Nagendra Prasad: review, validation, and proofreading. Mohammad Khalid and Shadma Wahab: resource and visualization. Harikaranahalli Puttaiah Shivaraju: conceptualization, methodology, supervision, writing, and proofreading – review & editing.

Conflicts of interest

The authors declare that they have no conflicts of interest.

Data availability

The data supporting the findings of this study are available within the article and its supplementary information (SI). Supplementary information is available. See DOI: **https://doi.org/10.1039/d5ma00914f**.

Additional data that support the study's conclusions are available from the corresponding author upon reasonable request.

Acknowledgements

The authors would like to thank the JSS Academy of Higher Education and Research, Mysuru, India for the research facility that provided access to electronic resources, CNMS-Jain

University, Bengaluru, for providing the XRD facility and electrochemical work station, and the Indian Institute of Science and Technology Roorkee, for XPS analysis. The authors extend their appreciation to the Deanship of Scientific Research at King Khalid University for funding this work through a large group Research Project under grant number RGP.2/274/45.

References

1 M. Joseph, M. Kumar, S. Haridas, C. Subrahmanyam and S. N. Remello, A review on the advancements of graphitic carbon nitride-based photoelectrodes for photoelectrochemical water splitting, *Energy Adv.*, 2024, **3**, 30–59.

2 J. Zhang, H. Ma and Z. Liu, Highly efficient photocatalyst based on all oxides WO3/Cu2O heterojunction for photoelectrochemical water splitting, *Appl. Catal., B*, 2017, **201**, 84–91.

3 J. Lin, X. Han, S. Liu, Y. Lv, X. Li and Y. Zhao, *et al.*, Nitrogen-doped cobalt-iron oxide cocatalyst boosting photoelectrochemical water splitting of BiVO4 photoanodes, *Appl. Catal., B*, 2023, **320**, 121947.

4 A. K. Vishwakarma, M. Hussain, S. K. Verma, V. Shukla, M. A. Shaz and O. N. Srivastava, Synthesis and characterizations of graphene/Sm doped BiFeO3 composites photoanode for efficient photo-electrochemical water splitting, *Int. J. Hydrogen Energy*, 2021, **46**(29), 15550–15560.

5 C. Li, Y. Wang, S. Chen, W. Zhang, Z. Wang and Z. Hou, Enhanced photoelectrochemical performance based on conformal and uniform ZnO/ZnSe/CdSe heterostructures on Zn foil substrate, *Int. J. Hydrogen Energy*, 2020, **45**(15), 8257–8272.

6 W. Wang, M. Xu, X. Xu, W. Zhou and Z. Shao, Perovskite oxide based electrodes for high-performance photoelectrochemical water splitting, *Angew. Chem., Int. Ed.*, 2020, **59**(1), 136–152.

7 R. Yukesh Kannah, S. Kavitha, Preethi, O. Parthiba Karthikeyan, G. Kumar and N. Vo Dai-Viet, *et al.*, Techno-economic assessment of various hydrogen production methods – A review, *Bioresour. Technol.*, 2021, **319**, 124175.

8 J. W. Yoon, J. H. Kim, H. W. Jang and J. H. Lee, *et al.*, NH2-MIL-125 (Ti)/TiO2 nanorod heterojunction photoanodes for efficient photoelectrochemical water splitting, *Appl. Catal., B*, 2019, **244**, 511–518.

9 C. Ding, J. Shi, Z. Wang and C. Li, Photoelectrocatalytic water splitting: significance of cocatalysts, electrolyte, and interfaces, *ACS Catal.*, 2017, **7**(1), 675–688.

10 R. Li, Latest progress in hydrogen production from solar water splitting via photocatalysis, photoelectrochemical, and photovoltaic-photoelectrochemical solutions, *Chin. J. Catal.*, 2017, **38**(1), 5–12.

11 W. H. Leng, P. R. F. Barnes, M. Juozapavicius, B. C. O'Regan and J. R. Durrant, Electron diffusion length in mesoporous nanocrystalline TiO2 photoelectrodes during water oxidation, *J. Phys. Chem. Lett.*, 2010, **1**(6), 967–972.

12 Z. Liu and X. Wang, Efficient photoelectrochemical water splitting of CaBi6O10 decorated with Cu2O and NiOOH for improved photogenerated carriers, *Int. J. Hydrogen Energy*, 2018, **43**(29), 13276–13283.

13 Z. Xie, D. Chen, J. Zhai, Y. Huang and H. Ji, Charge separation via synergy of homojunction and electrocatalyst in BiVO4 for photoelectrochemical water splitting, *Appl. Catal., B*, 2023, **334**, 122865.

14 J. Joy, J. Mathew and S. C. George, Nanomaterials for photoelectrochemical water splitting–review, *Int. J. Hydrogen Energy*, 2018, **43**(10), 4804–4817.

15 D. Ayodhya, Semiconductors-based Z-scheme materials for photoelectrochemical water splitting: A review, *Electrochim. Acta*, 2023, **448**, 142118.

16 D. Yu, Z. Liu, J. Zhang, S. Li, Z. Zhao and L. Zhu, *et al.*, Enhanced catalytic performance by multi-field coupling in KNbO3 nanostructures: Piezo-photocatalytic and ferro-photoelectrochemical effects, *Nano Energy*, 2019, **58**, 695–705.

17 H. S. Anusha, S. Yadav, T. Tenzin, J. S. Prabagar, K. M. Anilkumar and W. Kitirote, *et al.*, Improved CeMnO3 perovskite framework for visible-light-aided degradation of tetracycline hydrochloride antibiotic residue and methylene blue dye, *Int. J. Environ. Sci. Technol.*, 2023, **20**(12), 13519–13534.

18 N. Eswaramoorthy, L. Harikrishnan, Y. Selvaraj, A. P. Shyma, K. Lakshmanan and P. Rajesh, *et al.*, Eco-friendly carbon quantum dots from coffee waste: Improving charge transfer in solid-state perovskite solar cells, *Diamond Relat. Mater.*, 2025, **156**, 112386.

19 S. Kuppusamy, D. Selvakumaran, P. Rajaraman, K. Lakshmanan and M. K. Bin Ahmad, Development of surface-activated La0.6Ca0.4MnO3 perovskite-type electrodes using oxygen plasma for highly stable supercapacitor application, *Ceram. Int.*, 2024, **50**(24), 52695–52706.

20 K. Lakshmanan, P. Govindasamy, P. Govindasami, S. Marappan and L. Jintae, Facile synthesis of perovskite-type CeCuO3 nanoparticles as a robust bifunctional electrocatalyst for highly stable overall water-splitting, *J. Alloys Compd.*, 2025, **1014**, 178635.

21 M. C. Maridevaru, B. Aljafari, S. Anandan and M. Ashokkumar, Synergistic impacts of sonolysis aided photocatalytic degradation of water pollutant over perovskite-type CeNiO3 nanospheres, *New J. Chem.*, 2022, **46**(21), 10117–10127.

22 M. P. Harikrishnan, P. Naveena, N. Baskaran and A. C. Bose, Fabrication of cerium nickel oxide (CeNiO3) nanoparticle on vanadium tetra sulphide (VS4) nanosheet composite materials as an enhanced electrode for supercapacitor applications, *Electrochim. Acta*, 2023, **462**, 142729.

23 W. Yang, R. R. Prabhakar, J. Tan, S. D. Tilley and J. Moon, Strategies for enhancing the photocurrent, photovoltage, and stability of photoelectrodes for photoelectrochemical water splitting, *Chem. Soc. Rev.*, 2019, **48**(19), 4979–5015.

24 Y. Pihosh, I. Turkevych, K. Mawatari, T. Asai, T. Hisatomi and J. Uemura, *et al.*, Nanostructured WO3/BiVO4 photoanodes for efficient photoelectrochemical water splitting, *Small*, 2014, **10**(18), 3692–3699.

25 C. X. M. Ta, C. Akamoto, Y. Furusho and F. Amano, A macroporous-structured WO3/Mo-doped BiVO4 photoanode for vapor-fed water splitting under visible light irradiation, *ACS Sustainable Chem. Eng.*, 2020, **8**(25), 9456–9463.
26 S. S. Shenouda, T. H. AlAbdulaal, H. Y. Zahran and I. S. Yahia, Synthesis, structure identification and linear/nonlinear optics of hydrothermally grown WO3 nanostructured thin film/FTO: Novel approach, *Ceram. Int.*, 2022, **48**(6), 7663–7667.
27 M. Yang, T. Hang, C. Zhang, Y. Ma, H. Jiang and Q. Hao, *et al.*, Engineering a Tandem S-Scheme TiO2@ SrTiO3@ BiVO4 Photoanode for Superior PEC Water Oxidation, *Electrochim. Acta*, 2025, 147105.
28 M. J. Kim, C. Lee, Y. R. Jo, W. G. Jung, J. S. Ha and J. H. Shim, *et al.*, Amorphous Exsolution of Fe3O4 Nanoparticles in SrTiO3: A Path to High Activity and Stability in Photoelectrochemical Water-Splitting, *Small Struct.*, 2025, **6**(4), 2400450.
29 N. R. Reddy, A. S. Kumar, P. M. Reddy, R. R. Kakarla, J. H. Jung and T. M. Aminabhavi, *et al.*, Efficient synthesis of 3D ZnO nanostructures on ITO surfaces for enhanced photoelectrochemical water splitting, *J. Environ. Manage.*, 2024, **352**, 120082.
30 Y. Xie, Y. Sun, R. Jiang, J. Chang, Y. Yang and L. Zhang, *et al.*, Controllable synthesis of CdS nanospheres photoelectrode for photoelectrochemical water splitting, *Resour. Chem. Mater.*, 2024, **3**(1), 38–45.
31 N. Ahmad, F. Alharthi, M. Alam, R. Wahab, S. Manoharadas and B. Alrayes, Syngas production via CO_2 reforming of methane over $SrNiO_3$ and $CeNiO_3$ perovskites, *Energies*, 2021, **14**(10), 2928.
32 N. Baig, I. Kammakakam, W. Falath and I. Kammakakam, Nanomaterials: a review of synthesis methods, properties, recent progress, and challenges, *Mater. Adv.*, 2021, **2**(6), 1821–1871.
33 A. K. Tomar, G. Singh and R. K. Sharma, Charge storage characteristics of mesoporous strontium titanate perovskite aqueous as well as flexible solid-state supercapacitor cell, *J. Power Sources*, 2019, **426**, 223–232.
34 W. Gao, Z. Xia, F. Cao, J. C. Ho, Z. Jiang and Y. Qu, Comprehensive Understanding of the Spatial Configurations of CeO2 in NiO for the Electrocatalytic Oxygen Evolution Reaction: Embedded or Surface-Loaded, *Adv. Funct. Mater.*, 2018, **28**(11), 1706056, DOI: **10.1002/adfm.201706056**. [cited 2025 Oct 24].
35 N. Arjun, G. T. Pan and T. C. K. Yang, The exploration of Lanthanum based perovskites and their complementary electrolytes for the supercapacitor applications, *Results Phys.*, 2017, **7**, 920–926.
36 M. Kumar, J. H. Yun, V. Bhatt, B. Singh, J. Kim and J. S. Kim, *et al.*, Role of Ce3+ valence state and surface oxygen vacancies on enhanced electrochemical performance of single step solvothermally synthesized CeO2 nanoparticles, *Electrochim. Acta*, 2018, **284**, 709–720.
37 S. R. Gawali, D. P. Dubal, V. G. Deonikar, S. S. Patil, S. D. Patil and P. Gomez-Romero, *et al.*, Asymmetric supercapacitor based on nanostructured Ce-doped NiO (Ce: NiO) as positive and reduced graphene oxide (rGO) as negative electrode, *ChemistrySelect*, 2016, **1**(13), 3471–3478.
38 M. A. Peck and M. A. Langell, Comparison of nanoscaled and bulk NiO structural and environmental characteristics by XRD, XAFS, and XPS, *Chem. Mater.*, 2012, **24**(23), 4483–4490.
39 J. Zhu, H. Li, L. Zhong, P. Xiao, X. Xu and X. Yang, *et al.*, Perovskite oxides: preparation, characterizations, and applications in heterogeneous catalysis, *ACS Catal.*, 2014, **4**(9), 2917–2940.
40 J. S. Prabagar, T. Tenzin, S. Yadav, K. M. A. Kumar and H. P. Shivaraju, *et al.*, Facile synthesis of NdFeO3 perovskite for photocatalytic degradation of organic dye and antibiotic, *Mater. Today: Proc.*, 2023, **75**, 15–23.
41 Y. Wei, J. Su, X. Wan, L. Guo and L. Vayssieres, Spontaneous photoelectric field-enhancement effect prompts the low cost hierarchical growth of highly ordered heteronanostructures for solar water splitting, *Nano Res.*, 2016, **9**, 1561–1569.
42 S. Moscow, V. Kavinkumar, M. Sriramkumar, K. Jothivenkatachalam, P. Saravanan and N. Rajamohan, *et al.*, Impact of Erbium (Er) and Yttrium (Y) doping on BiVO4 crystal structure towards the enhancement of photoelectrochemical water splitting and photocatalytic performance, *Chemosphere*, 2022, **299**, 134343.
43 J. Liqiang, Q. Yichun, W. Baiqi, L. Shudan, J. Baojiang and Y. Libin, *et al.*, Review of photoluminescence performance of nano-sized semiconductor materials and its relationships with photocatalytic activity, *Sol. Energy Mater. Sol. Cells*, 2006, **90**(12), 1773–1787.
44 W. Zhang, Y. Ma, X. Zhu, S. Liu, T. An and J. Bao, *et al.*, Fabrication of Ag decorated g-C3N4/LaFeO3 Z-scheme heterojunction as highly efficient visible-light photocatalyst for degradation of methylene blue and tetracycline hydrochloride, *J. Alloys Compd.*, 2021, **864**, 158914.
45 Y. Li, Z. Hao, R. Wang, G. Wang, H. Li and C. Li, *et al.*, Interfacial electric field optimization and co-catalyst free LaFeO3-based pp-type homojunction for efficient PEC water splitting, *Chem. Eng. J.*, 2024, 149797.
46 R. B. Wei, P. Y. Kuang, H. Cheng, Y. B. Chen, J. Y. Long and M. Y. Zhang, *et al.*, Plasmon-enhanced photoelectrochemical water splitting on gold nanoparticle decorated ZnO/CdS nanotube arrays, *ACS Sustainable Chem. Eng.*, 2017, **5**(5), 4249–4257.
47 S. Khoomortezaei, H. Abdizadeh and M. R. Golobostanfard, Ferro-photocatalytic enhancement of photoelectrochemical water splitting using the WO3/BiFeO3 heterojunction, *Energy Fuels*, 2021, **35**(11), 9623–9634.
48 B. Huang, H. Wang, S. Liang, H. Qin, Y. Li and Z. Luo, *et al.*, Two-dimensional porous cobalt–nickel tungstate thin sheets for high performance supercapattery, *Energy Storage Mater.*, 2020, **32**, 105–114.
49 Z. H. Huang, F. F. Sun, Z. Y. Yuan, W. Sun, B. Jia and H. Li, *et al.*, An electro-activated bimetallic zinc-nickel hydroxide cathode for supercapacitor with super-long 140,000 cycle durability, *Nano Energy*, 2021, **82**, 105727.
50 M. P. Harikrishnan and A. C. Bose, Porous $CeNiO_3$ with an enhanced electrochemical performance and prolonged

cycle life (>50 000 cycles) via a lemon-assisted sol–gel autocombustion method, *New J. Chem.*, 2022, **46**(31), 15118–15129.

51 H. Arandiyan, S. S. Mofarah, Y. Wang, C. Cazorla, D. Jampaiah and M. Garbrecht, *et al.*, Impact of surface defects on LaNiO3 perovskite electrocatalysts for the oxygen evolution reaction, *Chem. – Eur. J.*, 2021, **27**(58), 14418–14426.

52 H. Khan, I. H. Lone, S. E. Lofland, K. V. Ramanujachary and T. Ahmad, Exploiting multiferroicity of TbFeO3 nanoparticles for hydrogen generation through photo/electro/photoelectro-catalytic water splitting, *Int. J. Hydrogen Energy*, 2023, **48**(14), 5493–5505.

53 W. Bai, Y. Zhou, G. Peng, J. Wang, A. Li and P. F. X. Corvini, Engineering efficient hole transport layer Ferrihydrite-MXene on BiVO4 photoanodes for photoelectrochemical water splitting: work function and conductivity regulated, *Appl. Catal., B*, 2022, **315**, 121606.

54 G. Liu, S. K. Karuturi, H. Chen, D. Wang, J. W. Ager and A. N. Simonov, *et al.*, Enhancement of the photoelectrochemical water splitting by perovskite BiFeO3 via interfacial engineering, *Sol. Energy*, 2020, **202**, 198–203.

55 D. Lee, A. Kvit and K. S. Choi, Enabling solar water oxidation by BiVO4 photoanodes in basic media, *Chem. Mater.*, 2018, **30**(14), 4704–4712.